Fernandes, V.M., and Roberts, G.G., 2020, Cretaceous to Recent net continental uplift from paleobiological data: Insights into sub-plate support: GSA Bulletin, https://doi.org/10.1130/B35739.1.

Supplemental Material

Dataset 1: [rawdata.csv]: Data downloaded from the PBDB website (https://paleobiodb.org), containing 580,346 fossil occurrences.

Dataset 2: [MeasuredUplift PBDB.txt]: Contains the 24,372 Cretaceous to Recent marine assemblages used to measure uplift, interpreted paleo-water depths and measured uplift.

Table S1: Comparison of paleobathymetric models.

Table S2: Benchmarking PBDB and independent paleoenvironments.

Figure S1: Simplified global sea-level compilation from Bessin et al. (2017).

Figure S2: Paleobathymetries for best-constrained samples.

Figure S3: Geophysical observations from the Western Interior of North America.

Figure S4: Geophysical observations from the Borborema Province, northeast Brazil.

Figure S5: Schematic illustrating lithospheric and asthenospheric columns used for isostatic calculations.

Figure S6: Comparison of a steady-state (equilibrated) and a disequilibrated geotherm on the generation of uplift by lithospheric thinning.

Table S3: Parameters used in isostatic calculations.

Supplemental Material for "Cretaceous to Recent Net Continental Uplift from Paleobiological Data: Insights into Sub-Plate Support"

Victoria M. Fernandes[1] and Gareth G. Roberts[1]

[1]*Department of Earth Science and Engineering, Imperial College London, South Kensington, SW7 2AZ, UK.*
Correspondence to: v.fernandes17@imperial.ac.uk, gareth.roberts@imperial.ac.uk.

This Supplemental Material contains additional text, five figures and three tables. The first section contains a description of the data used and generated by this study. These data are included separately as text files. The next section contains Tables S1 and S2, which show a comparison of paleobathymetric models, and a benchmark of environments from the Paleobiology Database (PBDB) against other paleoenvironmental analyses. The Figures S1 and S2 show the sea-level curves used in this study, and histograms of minimum, mean and maximum paleobathymetries. Figures S3 and S4 show geophysical data from western North America and the Borborema Province, Brazil. The final section expands on the methodology and parameters used to calculated topographic support, and includes Figure S5 and Table S3.

1 Datasets

Dataset 1 [rawdata.csv]: Data downloaded from the PBDB website (`https://paleobiodb.org`), containing 580,346 fossil occurrences. The dataset fields contain information about: Accepted taxon name, Collection number, Longitude, Latitude, Two letter country code, State, Maximum age (Ma), Minimum age (Ma), Formation, Member, Lithology, Depositional Environment, Tectonic Setting, Geology comments and Primary reference.

Dataset 2 [MeasuredUplift_PBDB.txt]: Contains the 24,372 Cretaceous to Recent marine assemblages used to measure uplift, interpreted paleo-water depths and measured uplift. We note that references for each sample can be obtained from the raw PBDB inventory, which is included as a separate text file. The dataset fields contain information about: Longitude, Latitude, Identifier number, Mean Age (Ma), Minimum Age (Ma), Maximum Age (Ma), Mean Paleo-water Depth (PWD, km), Minimum PWD (km), Maximum PWD (km), Formation, Depositional Environment, Geology comments, Tag (a/b/c; see main text), Mean Elevation (km), Minimum Elevation (km), Maximum Elevation (km), Mean sea-level (km), Minimum sea-level (km), Maximum sea-level (km), Mean uplift with no sea-level correction (km), Mean uplift (km), Minimum uplift (km), Maximum uplift (km).

2 Tables

Table S1: Comparison of paleobathymetric models.

Reference, Location	Environment & Description	B min [m]	B max [m]	PBDB Environment	No.	Tectonic Setting	B min [m]	B max [m]
Ziegler et al. (1985), Global	ocean trenches; turbidites or pelagic	6000	12000	deep-water indet.	10	none	250	4000
	ocean floor; pelagic sequence on ocean floor	4000	6000	basinal (silicicalstic)	3	none	500	4000
	continental slope-rise	200	4000	slope	34	none	250	4000
	prodelta fans	200	4000	basinal (silicicalstic)	3	none	500	4000
	outer shelf	50	200	offshore indet.	21	none	50	250
	prodelta	50	200	prodelta	29	none	15	100
	inner shelf	0	50	shoreface	33	none	1	50
	delta front	0	50	delta front	11	none	1	15
Sahagian and Jones (1993), Russian platform	shoreface; beach oolites, mudcracks, evaporites, fossils	0	2	shoreface	33	passive margin	1	150
	lagoon; mud, fossils	0	2	lagoonal	16	passive margin	0	2
	reef; fossils	0	2	reef, buildup or bioherm	30	passive margin	0	250
	transition zone; storm beds, fossils	2	10	transition zone/lower shoreface	37	passive margin	45	200
	offshore; fossils	10	25	offshore	20	passive margin	150	250
	deep; fossils	25	50	deep-water indet.	10	passive margin	250	4000
Sahagian et al. (1996), Russian Platform	deep water	100	200	deep-water indet.	10	passive margin	250	4000
Read (1985), Global	deep shelf and ramp; diverse open marine biota, upward fining, storm-generated beds, dominantly fair weather base	10	40	deep subtidal ramp	8	none	45	150
He et al. (2017), Pearl River Mouth	littoral; sea-level to fair weather-wave base	0	20	shallow subtidal indet.	32	passive margin	1	45
	inner shelf; fair to storm-wave base	20	100	deep subtidal indet.	7	passive margin	45	150
	outer shelf; storm-wave base to shelf break	100	200	offshore	20	passive margin	150	250
	continental slope; bathyal	200	3000	slope	34	passive margin	250	3000
	basin plain; abyssal	3000	5000	basinal (silicicalstic)	3	passive margin	2000	4000
Katz et al. (2013), New Jersey Shelf	upper shoreface	0	5	shallow subtidal indet.	32	passive margin	1	45
	lower shoreface	5	10	deep subtidal indet.	7	passive margin	45	150

	shoreface-offshore transition zone	10	30	transition zone/lower shoreface	37	passive margin	45	200
	inner neritic shelf	0	30	shoreface	33	passive margin	1	150
	middle-outer neritic shelf	30	200	offshore	20	passive margin	150	250
	offshore	20	200	offshore	20	passive margin	150	250
El-Azabi and El-Araby (2007), Gulf of Suez	foreshore intertidal	0	2	foreshore	13	rift	0	1
	shoreface / shallow subtidal	0	5	shallow subtidal indet.	32	rift	1	15
	deep subtidal	5	30	deep subtidal indet.	7	rift	15	50
	offshore transition zone	5	25	transition zone/lower shoreface	37	rift	15	70
	offshore; lower deep subtidal	25	30	offshore	20	rift	50	250
Short (2014), southern Australia Shelf	inner shelf; benthic species	0	70	shoreface	33	passive margin	1	150
	middle-outer shelf; benthic species	70	250	offshore	20	passive margin	150	250
	intertidal	0	3	foreshore	13	passive margin	0	1
	middle-deep neritic	60	140	offshore	20	passive margin	150	250
Allen (1970), modern Niger delta	delta front	0	30	delta front	11	passive margin	1	45
	prodelta	0	60	prodelta	29	passive margin	45	100
	nearshore/shoreface	0	20	shoreface	33	passive margin	1	150
	upper shoreface	0	7	shallow subtidal indet.	32	passive margin	1	45
	lower shoreface	7	20	deep subtidal indet.	7	passive margin	45	150
	offhsore	20	200	offshore	20	passive margin	150	250
	continental slope; bathyal	200	3000	slope	34	passive margin	250	3000
Adegoke et al. (2017), Niger delta	nearshore; includes shoreline, marsh and estuary	0	8	foreshore	13	passive margin	0	1
	marsh	0	8	marginal marine indet.	18	passive margin	0	45
	estuary	0	8	estuary/bay	12	passive margin	0	45
	inner neritic	8	55	shoreface	33	passive margin	1	150
	continental shelf	8	250	offshore	20	passive margin	150	250
	slope; bathyal	250	2000	slope	34	passive margin	250	3000
	basin floor; abyssal	2000	4000	basinal (siliciclastic)	3	passive margin	2000	4000
Davies et al. (2002), Arabian Plate	outer platform	50	200	offshore shelf	23	foreland basin	50	250

	middle platform	10	50	deep subtidal shelf	9	foreland basin	15	50
	inner platform	0	10	shallow subtidal indet.	32	foreland basin	1	15
Olson and Leckie (2003), northern Gulf of Mexico	marsh; benthic foraminifera zonations	0	5	marginal marine indet.	18	passive margin	0	45
	bay; benthic foraminifera zonations	0	5	estuary/bay	12	passive margin	0	45
	lagoon; benthic foraminifera zonations	0	5	lagoonal	16	passive margin	0	2
	inner neritic; benthic foraminifera zonations	0	50	shoreface	33	passive margin	1	150
	middle-outer neritic; benthic foraminifera zonations	50	150	offshore	20	passive margin	150	250
Brigaud et al. (2018), Paris basin	upper offshore; storm dominated, poorly sorted, bioturbation	10	40	transition zone/lower shoreface	37	cratonic basin	12	50
	shoal (shoreface); high energy, ooids, cross-bedding, well sorted	2	30	shoreface	33	cratonic basin	1	40
	lagoonal	0	2	lagoonal/ restricted shallow subtidal	17	cratonic basin	0	5
	intertidal; restricted and protected environment	0	2	peritidal	27	cratonic basin	0	2
	supratidal; brackish, brine ponds and episodic flux of normal marine waters	0	2	marginal marine indet.	18	cratonic basin	0	12

Table S2: Benchmarking PBDB and independent paleoenvironments.

Location	Age [Ma]	Stratigraphy	Reference, Environment	Benchmark Reference, Environment
Saudi Arabia; 46.824, 25.203	83.5–70.6	Hajajah Mb, Aruma Fm	*El-Sorogy et al.* (2016): basin reef, intra-shelf basin.	*Gameil et al.* (2020): intra-shelf basin reef, fore-reef, back-reef – based on fossils (corals, solitary corals, bivalves, rudists, gastropods, echinoids).
Skane, Sweden; 12.816, 55.566	66–61.6	Stevens Klint Fm	*Bjerager et al.* (2010): basin reef, deep-water coral reef complex, reefs are 20 m high, 200 m long, formed on a first order paleo-seafloor high.	*Schøder and Surlyk* (2020): cool-water, coral-bryozoan mound complex within a chalk seaway continental platform – based on fossil assemblage and associated sediments.
Colorado, USA; −104.717, 38.283	100.5–93.9	Bridge Creek Limestone Mb, Greenhorn Limestone	*Elder* (1987): basinal carbonate, cratonic basin, chalky, very well indurated. Section C2 constitutes interbedded limestones and shales.	*Elderbak and Leckie* (2016): deposition in deep axis of Greenhorn seaway, in anoxic event – based on benthic and planktonic foraminifera.
England, −0.267, 51.950	99.6–93.5	Totternhoe Stone Mb, Zig Zag Chalk	*Newton* (1892): basinal carbonate.	*Woods* (2015): sea floor pelagic carbonate – based on foraminifera, coccoliths, sedimentology.
−110.094, 36.525	99.6–93.5	Mancos Shale	*Kirkland et al.* (1996): basinal siliciclastic, foreland basin.	*Leckie et al.* (1991): basinal to neritic (oxygen minimum zone) – based on kaolinite abundances, benthic and planktonic calcareous forams. Indicates deeper water at peak transgression, transition into arenaceous benthic foraminifera assemblage, hummocky cross-beds (below fair weather wave base = 5–15 m).
Bern, Swizer-land: 7.517, 46.867	20.44–15.97	Upper Marine Molasse, Belpberg Beds	*Kroh and Menkveld-Gfeller* (2006): sandstone, delta front.	*Schlunegger et al.* (1997): Foreland basin deltaic shoreface, offshore bay, nearshore, foreshore, shoreface with 0–130 m PWD (given in text) – based on sedimentology.
Alabama, USA; −85.317, 32.126	85.8–70.6	Blufftown	*Schwimmer et al.* (1993): estuary/bay, most likely back-barrier or estuarine settings during relatively high sea-level stands.	*Case and Schwimmer* (1988): back-barrier marine or estuarine environment, near-normal salinity, with considerable fluvial input, shallow – based on sedimentology.
Alberta, Canada; −110.470, 49.120	83.5–70.6	Dinosaur Park	*Eberth and Brinkman* (1997): mudstone, estuary/bay.	*Beavan and Russell* (1999): paralic with increasing marine influence, brackish water marginal marine – based on fossils (shark teeth, marine reptiles) and sedimentology (inclined heterolithic stratification, characterized by alternating sand, mud, and carbonaceous shale laminae, with localized ironstone concretion suggestive of a lateral accretion surface).

South Dakota, USA; −103.220, 43.270	99.6–93.5	Hartland shale, Greenhorn Fm	*Sageman and Bina* (1997): offshore, foreland basin. Deposited during widespread marine flooding of the Western Interior U.S., the Greenhorn Formation is renowned for its organic carbon-rich shales and limestone-marlstone cycles	*Sageman* (1989): offshore, low-energy anoxia occasionally oxygenated by storm events, cratonic basin – based on geochemical analysis, benthic fossil assemblages, other fossil associations (e.g. ammonites).
Alabama, USA; −87.475, 32.141	56–47.8	Bashi Mb, Hatchetigbee Bluff Fm	*Palmer and Brann* (1965): perireef or subreef.	*Gibson and Bybell* (1984): inner shelf deposits, inner to middle neritic – based on foraminifera and sedimentology (shelly glauconitic silt and very fine grained sand, commonly including a thin sequence of laminated silt and clay at the top).
New Mexico, USA; −105.893, 35.492	93.5–89.3	Carlile Shale, Blue Hill	*Coates and Kauffman* (1973): bafflestone, reef, buildup or bioherm.	*Shimada* (2006): Comparing to the laterally equivalent in Kansas. Offshore to nearshore – based on distribution of fossil fish and sedimentary structures.
Maryland, USA; −76.516, 38.531	13.82–11.62	Choptank, Drumcliff	*Shattuck* (1904): shoreface sandstone. Mollusk-dense pale yellow-brown to pale orange well-sorted sand. Sub-tropical to temperate, in a current-swept channel-like basin.	*Kidwell et al.* (2015): shoreface to marine shelf – based on fossil assemblage (sedimentary structures are rare/absent). Densely packed shells and fine sand, onshore portions of a marine shelf, including sandy and shelly seafloors of a few meters to 10–20 m PWD (given in text).
Arizona, USA; −110.819, 35.745	93.5–89.3	Toreva Fm, Blue Point Tongue	*Kirkland et al.* (1996): transition zone/lower shoreface, foreland basin.	*Olesen* (1991): shoreface – based on sedimentology and fossils. Fine-grained, non-calcareous sandstone, stratification obscured by bioturbation but consists of small-scale, very low angle, planar-tabular cross-bedding or ripple laminations.

3 Figures

Sea Level Curve

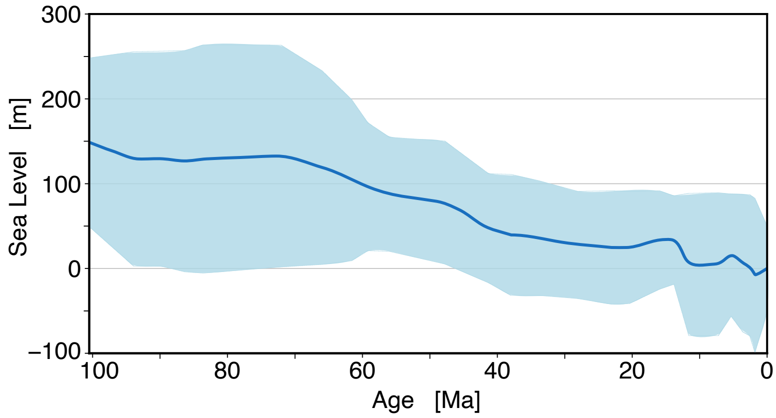

Figure S1: Simplified global sea-level compilation from *Bessin et al.* (2017). Solid blue curve is mean sea-level, light blue band indicates minimum and maximum values. These curves were used to correct uplift estimates using Equation 1 in the main manuscript.

Paleobathymetry Histograms

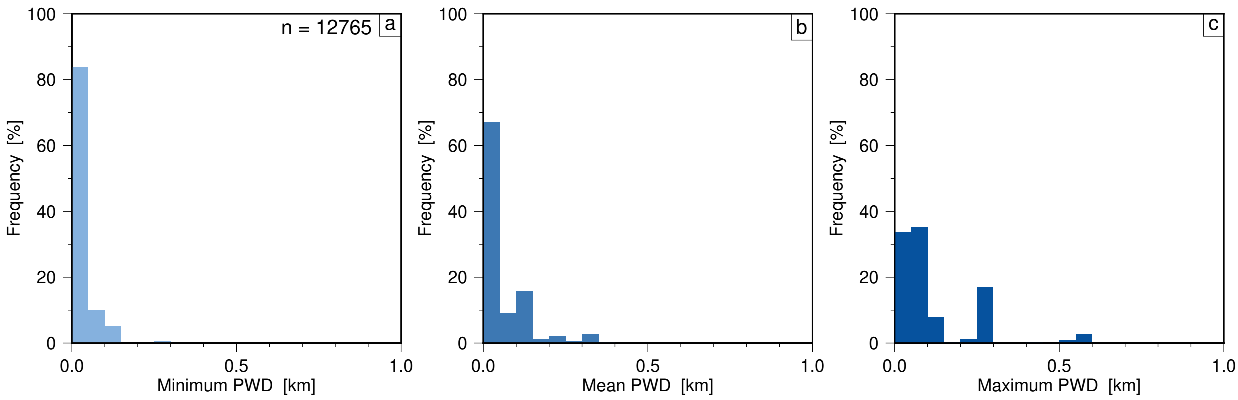

Figure S2: Paleobathymetries for best-constrained samples. (a) Minimum paleo-water depth (PWD), (b) mean and (c) maximum. These histograms exclude samples with tag ‘a’ and identified as ‘*marine indet.*’, ‘*carbonate indet.*’ or ‘*deep-water indet.*’. See body text of main manuscript for discussion of these results.

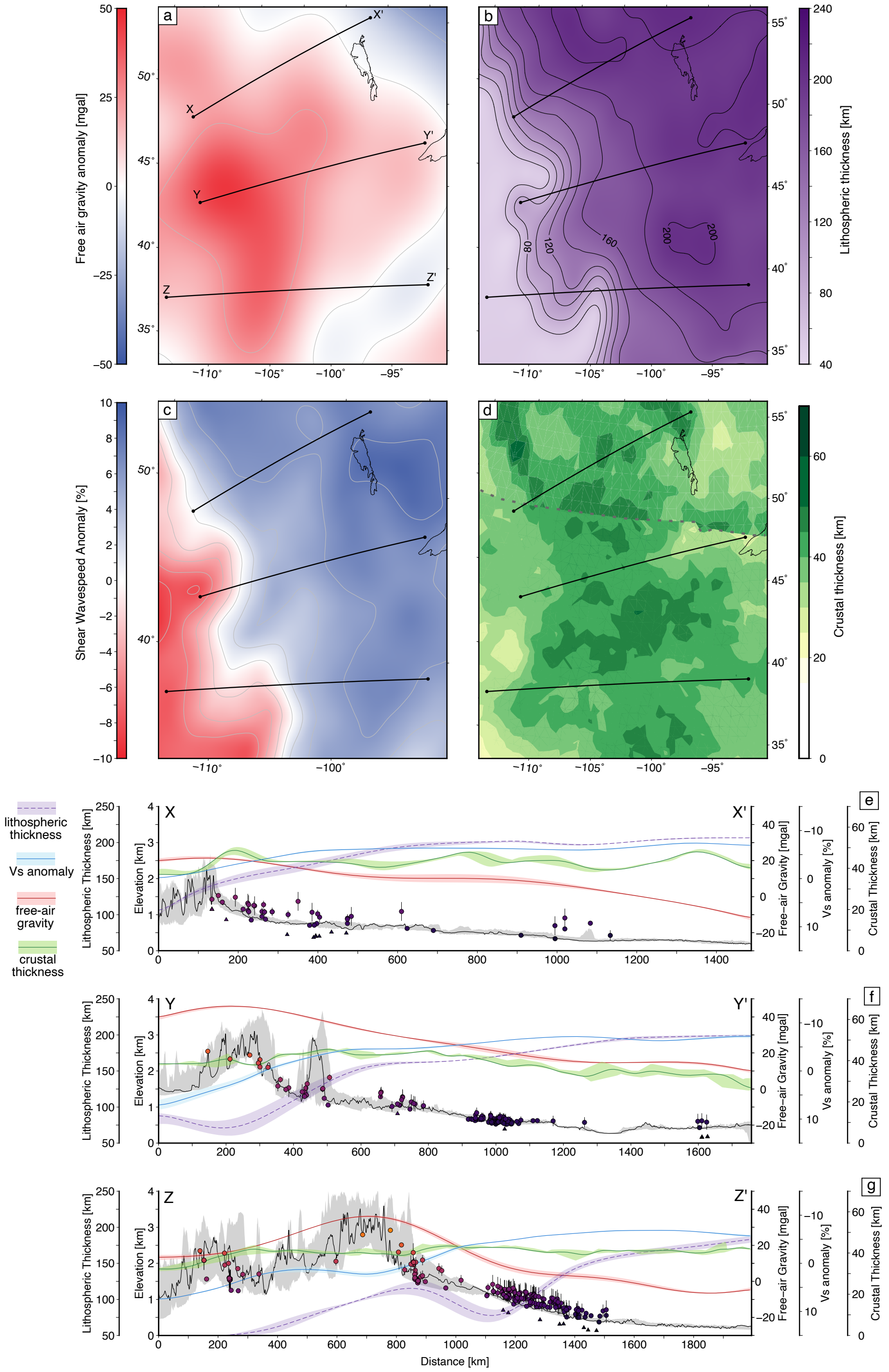

Figure S3: Geophysical observations from the Western Interior of North America. (a) Long wavelength free-air gravity (GRACE; $\sim 800-2500$ km band pass filter; *Tapley et al.*, 2005). (b) Lithospheric thickness from CAM2016 model (*Priestley and McKenzie*, 2013). (c) Shear-wavespeed anomaly at 100 km depth (SL2013sv; *Schaeffer and Lebedev*, 2013). (d) Crustal thickness from PnUS model (south of dotted gray line *Buehler and Shearer*, 2016) and CRUST1.0 (north of dotted gray line *Laske et al.*, 2013). Black curves show locations of cross sections X–X′, Y–Y′ and Z–Z′ (see Figure 6 in main text). (e–g) Cross sections X–X′, Y–Y′ and Z–Z′ showing topography from ETOPO1 (black curve), topography within 100 km wide swath (gray band), mean uplift of points within swath (colored circles). Mean and extrema of geophysical observations are shown along the swaths as colored curves and bands (see key).

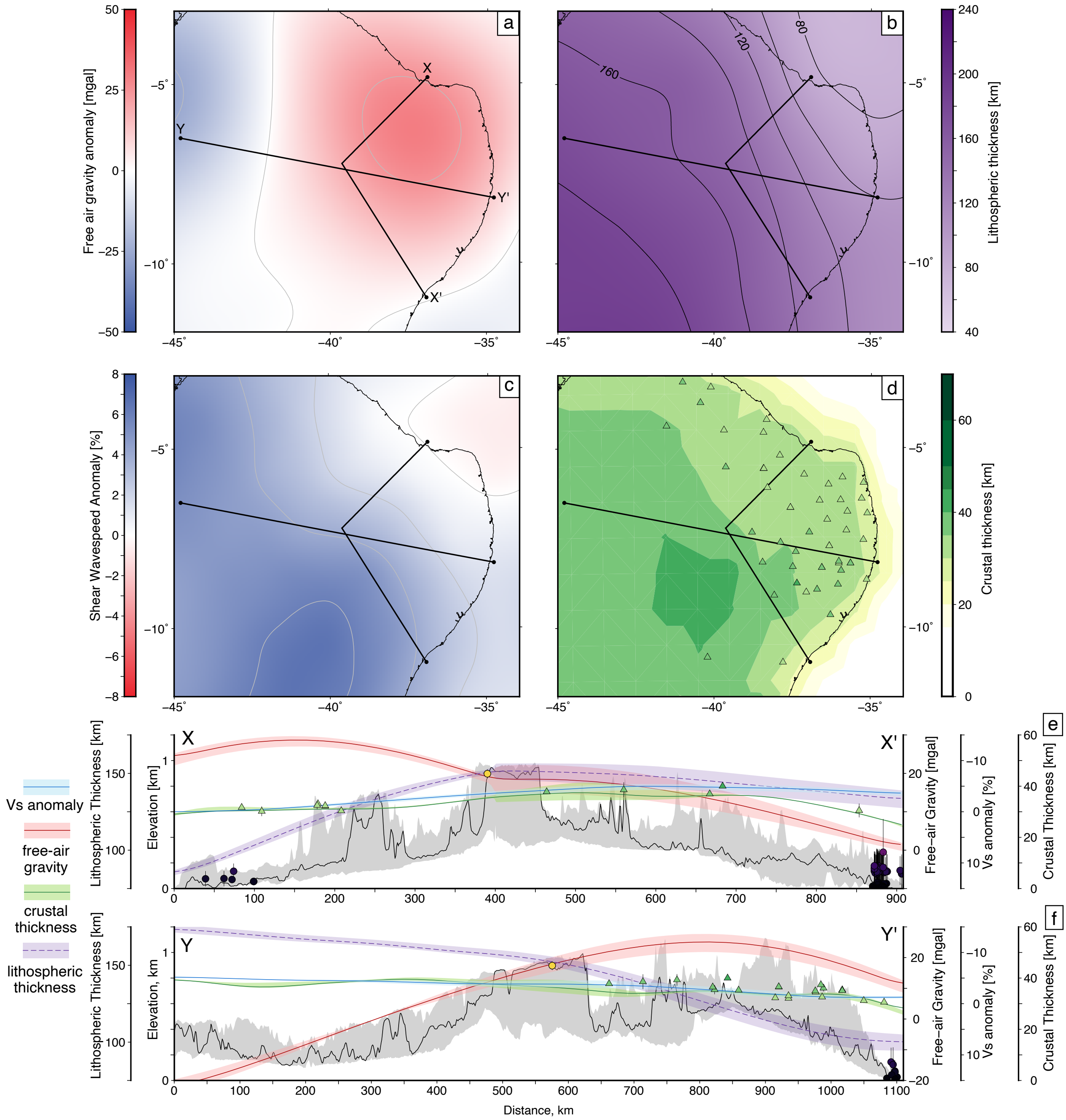

Figure S4: Geophysical observations from the Borborema Province, northeast Brazil. (a–f) Geophysical models are the same as those shown in Figure S3 of this document.

4 Isostatic calculations

In the main manuscript we compare present-day elevations and paleobathymetries of PaleoDB points to those predicted by isostatic calculations. Here, we describe the methodology in further detail. Figure S5 shows a schematic that describes the model setup. Values for all parameters used are defined in Table 1.

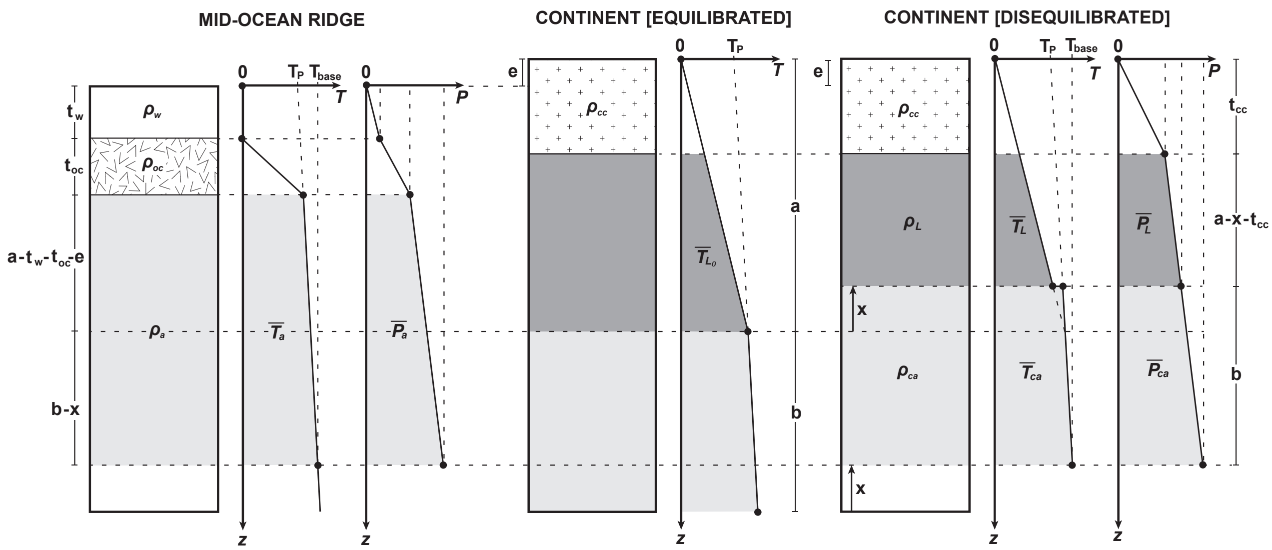

Figure S5: Schematic illustrating lithospheric and asthenospheric columns used for isostatic calculations. T, P, ρ, z refer to temperatures, pressures, densities and depths, respectively. Symbols, parameter values and units are defined in Table S3.

We explore the effects of lithospheric thinning and excess asthenospheric temperatures on the expected elevation of continents (*McNab et al.*, 2018; *Klöcking et al.*, 2018). Assuming isostasy prevails, the expected elevation, e, of a column of lithospheric material and associated asthenospheric mantle with respect to the depth of a standard mid-ocean ridge is given by

$$e = t_{cc}\left(\frac{\rho_L - \rho_{cc}}{\rho_a}\right) - t_w\left(\frac{\rho_a - \rho_w}{\rho_a}\right) - t_{oc}\left(\frac{\rho_a - \rho_{oc}}{\rho_a}\right) + (a - x)\left(\frac{\rho_a - \rho_L}{\rho_a}\right) + b\left(\frac{\rho_a - \rho_{ca}}{\rho_a}\right) \quad (1)$$

where b is the thickness of asthenospheric mantle that contributes to uplift and x the thickness of lithospheric mantle removed. We assume that e is small compared to a. The density of asthenospheric mantle beneath a mid-ocean ridge, ρ_a, is estimated by accounting for its temperature dependence. Assuming a linear adiabatic temperature gradient and accounting for compressibility

$$\rho_a = \rho_\circ\left(1 - \alpha\overline{T_a} + \frac{\overline{P_a}}{K}\right), \quad (2)$$

where the average temperature of oceanic asthenosphere, $\overline{T_a}$, is given by

$$\overline{T_a} = T_{base} - \frac{1}{2}\frac{\mathrm{d}T}{\mathrm{d}z}(a - t_w - t_{oc} + b - x), \quad (3)$$

and the temperature at the base of the column, T_{base}, is given by

$$T_{base} = T_P + (a + b - x)\frac{\mathrm{d}T}{\mathrm{d}z}. \quad (4)$$

The average lithostatic pressure of oceanic asthenosphere, $\overline{P_a}$, is given by

$$\overline{P_a} = \frac{g(\rho_w t_w + \rho_{oc} t_{oc})}{1000} + \frac{1}{2}\frac{\mathrm{d}P}{\mathrm{d}z}(a - t_w - t_{oc} + b - x). \tag{5}$$

Instantaneous removal of the base of continental lithosphere leaves the remaining portion thermally disequilibrated. When nothing (i.e. $x = 0$) has been removed the lithosphere is assumed to be thermally equilibrated (i.e. a steady-state geotherm, $\partial^2 T/\partial z^2 = 0$, is assumed). By assuming a linear geotherm from the surface ($T = 0$°C) to the base of the lithosphere and by accounting for the effects of mantle depletion and compressibility, we estimate the density of the continental lithospheric mantle, ρ_l, to be

$$\rho_L = (\rho_\circ - \Delta\rho_d)\left(1 - \alpha\overline{T_L} + \frac{\overline{P_L}}{K}\right) \tag{6}$$

where $\Delta\rho_d$ is the density difference between normal and depleted lithospheric mantle, and the average pressure in the continental lithospheric mantle, $\overline{P_L}$, is given by

$$\overline{P_L} = \frac{g t_{cc} \rho_{cc}}{1000} + \frac{1}{2}\frac{\mathrm{d}P}{\mathrm{d}z}(a - x - t_{cc}). \tag{7}$$

The average temperature of continental lithospheric mantle, $\overline{T_L}$, is given by

$$\overline{T_L} = \frac{T_{L_\circ}}{2a}(a - x + t_{cc}) \tag{8}$$

and T_{L_0} is the temperature at the base of unthinned continental lithosphere, given by

$$T_{L_\circ} = T_P + a\left(\frac{\mathrm{d}T}{\mathrm{d}z}\right). \tag{9}$$

We also consider the effects of emplacing anomalously hot asthenospheric mantle of thickness b beneath continental lithosphere. For an excess temperature of ΔT, the asthenospheric mantle beneath the continent has a density of

$$\rho_{ca} = \rho_\circ\left(1 - \alpha(\overline{T_{ca}} + \Delta T) + \frac{\overline{P_{ca}}}{K}\right) \tag{10}$$

where the mean temperature of unheated continental asthenosphere, $\overline{T_{ca}}$, is given by

$$\overline{T_{ca}} = T_P + \left(a - x + \frac{b}{2}\right)\frac{\mathrm{d}T}{\mathrm{d}z} \tag{11}$$

and the average pressure of the asthenosphere, $\overline{P_{ca}}$, is given by

$$\overline{P_{ca}} = \frac{g\rho_{cc}t_{cc}}{1000} + \frac{\mathrm{d}P}{\mathrm{d}z}\left(a - x - t_{cc} + \frac{b}{2}\right). \tag{12}$$

These equations were combined with Equation 1 and measured uplift to infer geologic histories of western North America and the Borborema province in the main manuscript (see also Figures S3 and S4). It is straightforward to calculate uplift for a state-state (equilbrated) geotherm by modifying $\mathrm{d}T/\mathrm{d}z$ (Figure S6).

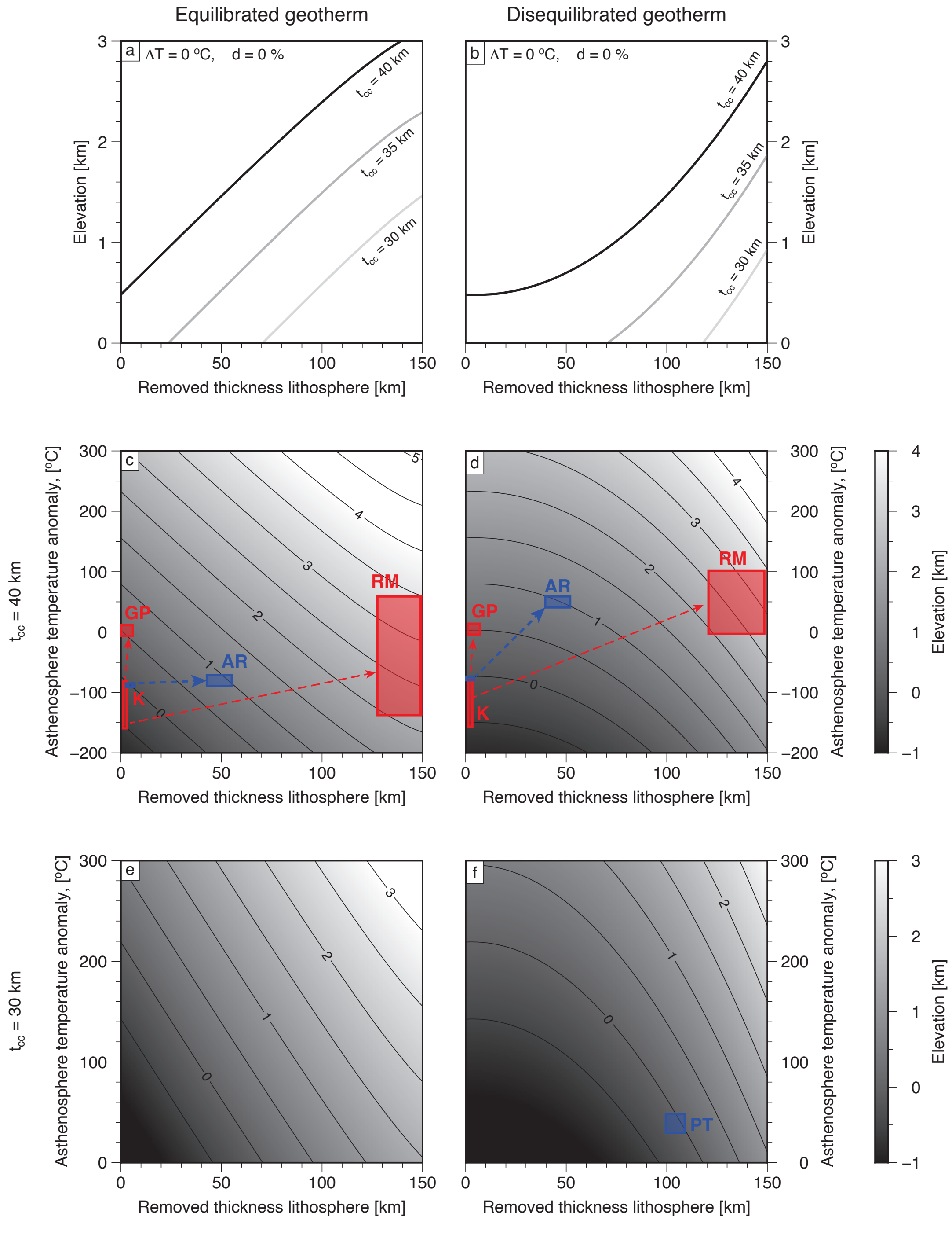

Figure S6: **Comparison of a steady-state (equilibrated) and a disequilibrated geotherm on the generation of uplift by lithospheric thinning**. Top row: predicted elevation as a function of removed thickness of lithosphere for a (a) steady-state and (b) disequilibrium lithospheric geotherm. Middle row: Gray scale and contours show calculated elevations for a crustal thickness of 40 km, and lithospheric thinning and asthenospheric thermal anomaly for a (c) steady-state and (d) disequilibrium geotherm. Bottom row: Predicted elevation for a crustal thickness of 30 km for a (e) steady-state and (f) disequilibrium geotherm. Labeled boxes indicate estimates of support for Cretaceous western interior of North America (K), Great Plains (GP), Araripe Plateau (AR), Rocky Mountains (RM), and Potiguar Basin (PT).

Table S3: Parameters used in isostatic calculations. MOR = Mid-oceanic ridge.

	Parameter	Symbol	Value	Units
MOR	Ridge depth	t_w	2.8	km
	Oceanic crust thickness	t_{oc}	7.1	km
	Water density	ρ_w	1.0	Mg m^{-3}
	Oceanic crust density	ρ_{oc}	2.86	Mg m^{-3}
	Oceanic asthenosphere density	ρ_a		Mg m^{-3}
	Oceanic asthenosphere average temperature	$\overline{T_a}$		°C
	Oceanic asthenosphere average pressure	$\overline{P_a}$		GPa
Continent	Elevation above sea-level	e		km
	Continental crust thickness	t_{cc}		km
	Original continental lithosphere thickness	a		km
	Removed lithospheric mantle thickness	x		km
	Thickness of hot asthenosphere	b	200	km
	Continental crust density	ρ_{cc}	2.75	Mg m^{-3}
	Continental lithospheric mantle density	ρ_L		Mg m^{-3}
	Lithospheric mantle depletion density	ρ_d		Mg m^{-3}
	Continental lithosphere average temperature	$\overline{T_L}$		°C
	Temperature at base of equilibrated lithosphere	$T_{L_\circ}$		°C
	Continental asthenosphere average temperature	$\overline{T_{ca}}$		°C
	Asthenospheric mantle temperature anomaly	ΔT		^{o}C
	Lithospheric mantle average pressure	$\overline{P_L}$		GPa
	Continental asthenosphere average pressure	$\overline{P_{ca}}$		GPa
General	Reference mantle density	$\rho_\circ$	3.33	Mg m^{-3}
	Mantle adiabatic temperature gradient	$\mathrm{d}T/\mathrm{d}z$	0.44	°C km^{-1}
	Mantle thermal expansion coefficient	α	3.3×10^{-5}	°C^{-1}
	Potential temperature of ambient mantle	T_P	1320	°C
	Temperature at base of column	T_{base}		°C
	Mantle pressure gradient	$\mathrm{d}P/\mathrm{d}z$	0.033	GPa km^{-1}
	Bulk Modulus	K	115.2	GPa
	Gravitational acceleration	g	9.8	m s^{-1}

References

Adegoke, O. S., Oyebamiji, A. S., Edet, J. J., Osterloff, P. L., and Ulu, O. K. eds., 2017, Foraminifera and Calcareous Nannofossil Biostratigraphy of the Niger Delta, Chapter 5 - Paleoenvironmental Synthesis: Elsevier, Oxford, UK, 129–144.

Allen, J. R. L., 1970, Sediments of the modern Niger delta: a summary and review, *in* Morgan, J. P. eds. Deltaic Sedimentation, Modern and Ancient, Special Publications of SEPM, pp. 138.

Beavan, N. R. and Russell, A. P., 1999, An Elasmobranch Assemblage from the Terrestrial-Marine Transitional Lethbridge Coal Zone (Dinosaur Park Formation: Upper Campanian), Alberta, Canada: Journal of Paleontology, v. 73 no. 3, p. 494–503, doi:10.1017/S0022336000028006.

Bessin, P., Guillocheau, F., Robin, C., Braun, J., Bauer, H., and Schroëtter, J., 2017, Quantification of vertical movement of low elevation topography combining a new compilation of global sea-level curves and scattered marine deposits (Armorican Massif, western France): Earth and Planetary Science Letters, v. 470, p. 25–36, doi:10.1016/j.epsl.2017.04.018.

Bjerager, M., Surlyk, F., Lykke-Andersen, H., Thibault, N., and Stemmerik, L., 2010, Danian cool-water coral reefs in southern Scandinavia localised over seafloor highs: Marine and Petroleum Geology, v. 27, p. 455–466.

Brigaud, B., Vincent, B., Pagel, M., Gras, A., Noret, A., Landrein, P. and Huret, E., 2018, Sedimentary architecture, depositional facies and diagenetic response to intracratonic deformation and climate change inferred from outcrops for a pivotal period (Jurassic/Cretaceous boundary, Paris Basin, France): Sedimentary geology, v. 373, p. 48–76.

Buehler J. S. and Shearer, P. M., 2016, Uppermost mantle seismic velocity structure beneath USArray: Journal of Geophysical Research, v. 121, doi:10.1002/2016JB013265.

Case, G. R. and Schwimmer, D. R., 1988, Late Cretaceous Fish from the Blufftown Formation (Campanian) in Western Georgia: Journal of Paleontology, v. 62 no. 2, p. 290–301.

Coates, A. G. and Kauffman, E. G., 1973, Stratigraphy, paleontology and paleoenvrionment of a Cretaceous coral thicket, Lamy, New Mexico: Journal of Paleontology, v. 47 no. 5, p. 953–968.

Davies, R. B., Casey, D. M., Horbury, A. D., Sarland, P. R., and Simmons, M. D., 2002, Early to Mid-Cretaceous mixed carbonate-siliciclastic shelfal systems: Examples, issues and models from the Arabian Plate: Geoarabia, v. 7 no. 3, p. 541–598.

Eberth, D. A. and Brinkman, D. B., 1997, Paleoecology of an estuarine, incised-valley fill in the Dinosaur Park Formation (Judith River Group, Upper Cretaceous) of southern Alberta, Canada: Palaios, v. 12, p. 43–58.

El-Azabi, M. and El-Araby, A., 2007, Depositional framework and sequence stratigraphic aspects of the Coniacian–Santonian mixed siliciclastic/carbonate Matulla sediments in Nezzazat and Ekma blocks, Gulf of Suez, Egypt: Journal of African Earth Sciences, v. 47, p. 179–202.

El-Sorogy, A. S., Ismail, A., Youssef, M., and Nour, H., 2016, Facies development and paleoenvironment of the Hajajah Limestone Member, Aruma Formation, central Saudi Arabia: Journal of African Earth Sciences, v. 124, 355–364.

Elder, W. P., 1987, The paleoecology of the Cenomanian-Turonian (Cretaceous) stage boundary extinctions at Black Mesa, Arizona: Palaios, v. 2 no. 1, p. 24–40.

Elderbak, K. and Leckie, M., 2016, Paleocirculation and foraminiferal assemblages of the Cenomanian–Turonian Bridge Creek Limestone bedding couplets: Productivity vs. dilution during OAE2: Cretaceous Research, v.60, p. 52–77.

Gameil, M., El-Sorogy, A. S. and Al-Kahtany, K., 2020, Solitary corals of the Campanian Hajajah Limestone Member, Aruma Formation, Central Saudi Arabia: Historical Biology, v. 32 no. 1, p. 1–17.

Gibson, T. G. and Bybell, L. M., 1984, Facies changes in the Hatchetigbee Formation in Alabama-Georgia and the Wilcox-Claiborne Group unconformity: Gulf Coast Association of Geological Societies Transactions, v. 31, p. 301–306.

He, M., Zhong, G., Liu, X., Liu, L., Shen, X., Wu, Z. and Huang, K., 2017, Rapid post-rift tectonic subsidence events in the Pearl River Mouth Basin, northern South China Sea margin: Journal of Asian Earth Sciences, v. 147, p. 271–283.

Katz, M. E., Browning, J. V., Miller, K. G., Monteverde, D. H., Mountain, G. S. and Williams, R. H., 2013, Paleobathymetry and sequence stratigraphic interpretations from benthic foraminifera: Insights on New Jersey shelf architecture, IODP Expedition 313: Geosphere, v. 9 no.6, p. 1488–1513.

Kidwell, S. M., Powars, D. S., Edwards, L. E., and Vogt, P. R., 2015, Miocene Stratigraphy and Paleoenvironments of the Calvert Cliffs, Maryland *in* Brezinski, D. K., Halka, J. P., and Ortt Jr., R. A. eds., Tripping from the Fall Line, Field Guide (Geological Society of America), v. 40, p. 231–279.

Kirkland, J. I., 1996, Paleontology of the Greenhorn cylcothem (Cretaceous: late Cenomanian to middle Turonian) at Black Mesa, northeastern Arizona: New Mexico Museum of Natural History and Science Bulletin, v. 9, p. 1–131.

Klöcking, M., White, N. J., Maclennan, J., McKenzie, D., and Fitton, J. G., 2018, Quantitative Relationships Between Basalt Geochemistry, Shear Wave Velocity, and Asthenospheric Temperature Beneath Western North America: Geochemistry, Geophysics, Geosystems, v. 19 no. 9, p. 3376–3404, doi:10.1029/2018GC007559.

Kroh, A. and Menkveld-Gfeller, U., 2006, Echinoids from the Belpberg Beds (Obere Meeresmolasse, Middle Burdigalian) in the area of Bern (Switzerland): Eclogae geologicae Helvetiae, v. 99, p. 193–203.

Laske, G., Masters, G., Ma, Z., and Pasyanos, M., 2013, Update on CRUST1.0–A 1-degree global model of Earth's crust: GU General Assembly Geophysical Research Abstracts, v. 15, p. 2658, Vienna, Austria.

Leckie, R. M., Schmidt, M. G. Finkelstein, D. and Yuretich, R., 1991, Paleoceanographic and paleoclimatic interpretations of the Mancos Shale (Upper Cretaceous), Black Mesa Basin, Arizona *in* Nationa, J. D. and Eaton, J. G. eds., Stratigraphy, Depositional Environments, and Sedimentary Tectonics of the Western Margin, Cretaceous Western Interior Seaway, Geological Society of America Special Paper 260.

Luz, R. M. N., Julià, J. and do Nascimento, A. F., 2015a, Crustal structure of the eastern Borborema Province, NE Brazil, from the joint inversion of receiver functions and surface wave dispersion: Implications for plateau uplift: Journal of Geophysical Research – Solid Earth, v. 120, p. 3848–3869, doi:10.1002/2015JB011872.

McNab, F., Ball, P. W., Hoggard, M. J., and White, N. J., 2018, Neogene uplift and magmatism of Anatolia: Insights from drainage analysis and basaltic geochemistry: Geochemistry, Geophysics, Geosystems, v. 19 no. 1, p. 175–213, doi:10.1002/2017GC007251.

Newton, E. T., 1892, Note on an iguanodont tooth from the lower Chalk ("Totternhoe Stone"), near Hitchin: *Geological Magazine, new series*, v. 3 no. 9, p. 49–50.

Olesen, J., 1991, Foraminiferal biostratigraphy and paleoecology of the Mancos Shale (Upper Cretaceous), southwestern Black Mesa, Arizona, *in* Nationa, J. and Eaton J. G. eds., Stratigraphy, Depositional Environments, and Sedimentary Tectonics of the Western Margin, Cretaceous Western Interior Seaway, Geological Society of America Special Paper, 260, p. 153–166.

Olson, H. C., and Keckie, R. M., 2003, Foraminifera as proxies for sea-level change on siliciclastic margins: *SEPM Special Publication*, v. 74, p. 5–19.

Palmer, K. V., and Brann, D. C., 1965, Catalogue of the Paleocene and Eocene mollusca of the southern and eastern United States. Part 1: Pelecypoda–Amphineura–Peteropoda–Scaphopoda and Cephalopoda: *Bulletins of American Paleontology*, v. 48, p. 1–471.

Priestley, K., and McKenzie, D., 2013, The relationship between shear wave velocity, temperature, attenuation and viscosity in the shallow part of the mantle: Earth and Planetary Science Letters, v. 381, p. 78–91, doi:10.1016/j.epsl.2013.08.022.

Read, J. F., 1985, Carbonate Platform Facies Models: APPG Bulletin, v. 69 no. 1, p. 1–21.

Sageman, B. B, 1989, The benthic boundary biofacies model: Hartland Shale Member, Greenhorn Formation (Cenomanian), Western Interior, North America: Paleogeography, Paleoclimatology, Paleoecology, v. 74, p. 87–110.

Sageman, B. S. and Bina, C. R., 1997, Diversity and Species Abundance Patterns in Late Cenomanian Black Shale Biofacies–Western Interior–U.S.: Palaios, v. 12, p. 449–466.

Sahagian, D. and Jones, M., 1993, Quantified Middle Jurassic to Paleocene eustatic variations based on Russian Platform stratigraphy: Stage level resolution: Geological Society of America Bulletin, v. 105 no. 8, p. 1109–1118.

Sahagian, D., Pinous, O., Olferiev, A. and Zakharov, V., 1996, Eustatic curve for the Middle Jurassic—Cretaceous based on Russian Platform and Siberian stratigraphy: Zonal resolution: AAPG bulletin, v. 80 no. 9, p. 1433–1458.

Schaeffer, A. J. and Lebedev, S., 2013, Global shear speed structure of the upper mantle and transition zone: Geophysical Journal International, v. 149, p. 417–449, doi:10.1093/gji/ggt095.

Schlunegger, F., Leu, W. and Matter, A., 1997, Sedimentary Sequences, Seismic Facies, Subsidence Analysis, and Evolution of the Burdigalian Upper Marine Molasse Group, Central Switzerland: AAPG Bulletin, v. 81 no. 7, p. 1185–1207.

Schøder, A. E. and Surlyk, F., 2020, Adaptive brachiopod morphologies in four key environments of the Late Cretaceous–Danian Chalk Sea of Northern Europe: A comparative study: Cretaceous Research, v. 107, 104288, doi:10.1016/j.cretres.2019.104288.

Schwimmer, D. R., Williams, G. D., Dobie, J. L., and Siesser, W. G., 1993, Late Cretaceous dinosaurs from the Blufftown Formation in western Georgia and eastern Alabama: Journal of Paleontology, v. 67 no. 2, p. 288–296.

Shattuck, G. B., 1904, Geological and paleontological relations–with a review of earlier investigations: Maryland Geological Survey.

Shimada, K., 2006, Marine vertebrates from the Blue Hill Shale member of the Carlile Shale (Upper Cretaceous: Middle Turonian) in Kansas, *in* Lucas, S. G. and Sullivan, R. M. eds., Late Cretaceous vertebrates from the Western Interior, New Mexico Museum of Natural History and Science Bulletin, v. 35, p. 165–176.

Short, A. D., 2014, Australia's temperate carbonate coast: Sources, depositional environments and implications: Geological Society London, Special Publications, v. 388 no. 1, p. 389–405.

Tapley, B., Ries, J., Bettadpur, S., Chambers, D., Cheng, M., Condi, F., Gunter, B., Kang, Z., Nagel, P., Pastor, R., et al., 2005, GGM02 – An improved Earth gravity field model from GRACE: Journal of Geodesy, v. 79, p. 467–478, doi:10.1007/s00190-005-0480-z.

Woods, M. A, 2015, Applied paleontology in the Chalk Group: Quality control for geological mapping and modelling and revealing new understanding: Proceedings of the Geologists' Association, v. 126 no. 6, p. 777–787.

Ziegler, A., Rowley, D., Lottes, A., Sahagian, D., Hulver, M. and Gierlowski, T., 1985, Paleogeographic interpretation: with an example from the mid-Cretaceous: Annual Reviews of Earth and Planetary Science, v. 13, p. 385–425, doi:10.1146/annurev.earth.13.1.385.